Research Article | Vol. 25, No. 13 | 26 Jun 2017 | OPTICS EXPRESS 14494
Optics EXPRESS

Graphene on meta-surface for super-resolution optical imaging with a sub-10 nm resolution

SHUN CAO,[1,2] TAISHENG WANG,[1] QIANG SUN,[1,5] BINGLIANG HU,[3] URIEL LEVY,[4] AND WEIXING YU[3,*]

[1]*State Key Laboratory of Applied Optics, Changchun Institute of Optics, Fine Mechanics & Physics, Chinese Academy of Sciences, No.3888, Dongnanhu Road, Changchun, Jilin, China*
[2]*University of the Chinese Academy of Sciences, Beijing 10039, China*
[3]*Key Laboratory of Spectral Imaging Technology, Xi'an Institute of Optics and Precision Mechanics, Chinese Academy of Sciences, No.17, Xinxi Road, Xian 710119, China*
[4]*Department of Applied Physics, The Benin School of Engineering and Computer Science, The Center for Nanoscience and Nanotechnology, The Hebrew University of Jerusalem, Jerusalem 91904, Israel*
[5]*sunq@ciomp.ac.cn*
**yuwx@opt.ac.cn*

Abstract: Nowadays, wide-field of view plasmonic structured illumination method (WFPSIM) has been extensively studied and experimentally demonstrated in biological researches. Normally, noble metal structures are used in traditional WFPSIM to support ultra-high wave-vector of SPs and an imaging resolution enhancement of 3-4 folds can be achieved. To further improve the imaging resolution of WFPSIM, we hereby propose a wide-field optical nanoimaging method based on a hybrid graphene on meta-surface structure (GMS) model. It is found that an ultra-high wave-vector of graphene SPs can be excited by a metallic nanoslits array with localized surface plasmon enhancement. As a result, a standing wave surface plasmons (SW-SPs) interference pattern with a period of 11 nm for a 980 nm incident wavelength can be obtained. The potential application of the GMS for wide-field of view super-resolution imaging is discussed followed by simulation results which show that an imaging resolution of sub-10 nm can be achieved. The demonstrated method paves a new route for wide field optical nanoimaging, with applications e.g. in biological research to study biological processes occurring in cell membrane.

OCIS codes: (100.6640) Superresolution; (160.3918) Metamaterials; (240.6680) Surface plasmons.

References and links

1. H. Raether, *Surface Plasmons on Smooth and Rough Surfaces and Gratings* (Springer Berlin Heidelberg, 1988).
2. E. Ozbay, "Plasmonics: merging photonics and electronics at nanoscale dimensions," Science **311**(5758), 189–193 (2006).
3. A. Polman and H. A. Atwater, "Plasmonics: optics at the nanoscale," Mater. Today **8**(1), 56 (2005).
4. J. N. Anker, W. P. Hall, O. Lyandres, N. C. Shah, J. Zhao, and R. P. Van Duyne, "Biosensing with plasmonic nanosensors," Nat. Mater. **7**(6), 442–453 (2008).
5. N. Li, A. Tittl, S. Yue, H. Giessen, C. Song, B. Ding, and N. Liu, "DNA-assembled bimetallic plasmonic nanosensors," Light Sci. Appl. **3**(12), e226 (2014).
6. Z. Liu, J. M. Steele, W. Srituravanich, Y. Pikus, C. Sun, and X. Zhang, "Focusing surface plasmons with a plasmonic lens," Nano Lett. **5**(9), 1726–1729 (2005).
7. X. Hao, C. Kuang, Z. Gu, Y. Wang, S. Li, Y. Ku, Y. Li, J. Ge, and X. Liu, "From microscopy to nanoscopy via visible light," Light Sci. Appl. **2**(10), e108 (2013).
8. Z. Liu, S. Durant, H. Lee, Y. Pikus, N. Fang, Y. Xiong, C. Sun, and X. Zhang, "Far-field optical superlens," Nano Lett. **7**(2), 403–408 (2007).
9. A. Yanai and U. Levy, "Subdiffraction-limited imaging based on longitudinal modes in a spatially dispersive slab," Phys. Rev. B **90**(7), 075107 (2014).
10. J. B. Pendry, "Negative refraction makes a perfect lens," Phys. Rev. Lett. **85**(18), 3966–3969 (2000).
11. N. Fang, H. Lee, C. Sun, and X. Zhang, "Sub-diffraction-limited optical imaging with a silver superlens," Science **308**(5721), 534–537 (2005).

#290619 https://doi.org/10.1364/OE.25.014494
Journal © 2017 Received 20 Mar 2017; revised 3 Jun 2017; accepted 8 Jun 2017; published 16 Jun 2017

Optics EXPRESS

12. Z. Liu, H. Lee, Y. Xiong, C. Sun, and X. Zhang, "Far-field optical hyperlens magnifying sub-diffraction-limited objects," Science **315**(5819), 1686 (2007).
13. E. Chung, Y.-H. Kim, W. T. Tang, C. J. R. Sheppard, and P. T. C. So, "Wide-field extended-resolution fluorescence microscopy with standing surface-plasmon-resonance waves," Opt. Lett. **34**(15), 2366–2368 (2009).
14. A. Sentenac, K. Belkebir, H. Giovannini, and P. C. Chaumet, "High-resolution total-internal-reflection fluorescence microscopy using periodically nanostructured glass slides," J. Opt. Soc. Am. A **26**(12), 2550–2557 (2009).
15. P. S. Tan, X. C. Yuan, G. H. Yuan, and Q. Wang, "High-resolution wide-field standing-wave surface plasmon resonance fluorescence microscopy with optical vortices," Appl. Phys. Lett. **97**(24), 241109 (2010).
16. Q. Wang, J. Bu, P. S. Tan, G. H. Yuan, J. H. Teng, H. Wang, and X.-C. Yuan, "Subwavelength-sized plasmonic structures for wide-field optical microscopic imaging with super-resolution," Plasmonics **7**(3), 427–433 (2012).
17. F. Wei and Z. Liu, "Plasmonic structured illumination microscopy," Nano Lett. **10**(7), 2531–2536 (2010).
18. F. Wei, D. Lu, H. Shen, W. Wan, J. L. Ponsetto, E. Huang, and Z. Liu, "Wide field super-resolution surface imaging through plasmonic structured illumination microscopy," Nano Lett. **14**(8), 4634–4639 (2014).
19. A. Sentenac, K. Belkebir, H. Giovannini, and P. C. Chaumet, "Subdiffraction resolution in total internal reflection fluorescence microscopy with a grating substrate," Opt. Lett. **33**(3), 255–257 (2008).
20. B. Gjonaj, A. David, Y. Blau, G. Spektor, M. Orenstein, S. Dolev, and G. Bartal, "Sub-100 nm focusing of short wavelength plasmons in homogeneous 2D space," Nano Lett. **14**(10), 5598–5602 (2014).
21. Y. Xiong, Z. Liu, and X. Zhang, "Projecting deep-subwavelength patterns from diffraction-limited masks using metal-dielectric multilayers," Appl. Phys. Lett. **93**(11), 111116 (2008).
22. Z. Jacob, L. V. Alekseyev, and E. Narimanov, "Optical hyperlens: far-field imaging beyond the diffraction limit," Opt. Express **14**(18), 8247–8256 (2006).
23. W. L. Gao, F. Z. Fang, Y. M. Liu, and S. Zhang, "Chiral surface waves supported by biaxial hyperbolic metamaterials," Light Sci. Appl. **4**(9), e328 (2015).
24. P. A. Belov and Y. Hao, "Subwavelength imaging at optical frequencies using a transmission device formed by a periodic layered metal-dielectric structure operating in the canalization regime," Phys. Rev. B **73**(11), 113110 (2006).
25. Y. Xiong, Z. Liu, C. Sun, and X. Zhang, "Two-dimensional imaging by far-field superlens at visible wavelengths," Nano Lett. **7**(11), 3360–3365 (2007).
26. S. Cao, T. Wang, W. Xu, H. Liu, H. Zhang, B. Hu, and W. Yu, "Gradient permittivity meta-structure model for wide-field super-resolution imaging with a sub-45 nm resolution," Sci. Rep. **6**(1), 23460 (2016).
27. S. Cao, T. Wang, Q. Sun, B. Hu, and W. Yu, "Meta-nanocavity model for dynamic super-resolution fluorescent imaging based on the plasmonic structure illumination microscopy method," Opt. Express **25**(4), 3863–3874 (2017).
28. A. Vakil and N. Engheta, "Transformation optics using graphene," Science **332**(6035), 1291–1294 (2011).
29. V. Apalkov and M. I. Stockman, "Proposed graphene nanospaser," Light Sci. Appl. **3**(7), e191 (2014).
30. Z. Fei, A. S. Rodin, G. O. Andreev, W. Bao, A. S. McLeod, M. Wagner, L. M. Zhang, Z. Zhao, M. Thiemens, G. Dominguez, M. M. Fogler, A. H. Castro Neto, C. N. Lau, F. Keilmann, and D. N. Basov, "Gate-tuning of graphene plasmons revealed by infrared nano-imaging," Nature **487**(7405), 82–85 (2012).
31. L. Ju, B. Geng, J. Horng, C. Girit, M. Martin, Z. Hao, H. A. Bechtel, X. Liang, A. Zettl, Y. R. Shen, and F. Wang, "Graphene plasmonics for tunable terahertz metamaterials," Nat. Nanotechnol. **6**(10), 630–634 (2011).
32. N. Papasimakis, S. Thongrattanasiri, N. I. Zheludev, and F. J. García de Abajo, "The magnetic response of graphene split-ring metamaterials," Light Sci. Appl. **2**(7), e78 (2013).
33. S.-A. Biehs, G. S. Agarwal, "Large enhancement of Förster resonance energy transfer on graphene platforms," Appl. Phys. Lett. **103**(24), 243112 (2013).
34. K. A. Velizhanin and T. V. Shahbazyan, "Long-range plasmon-assisted energy transfer over doped graphene," Phys. Rev. B **86**(24), 245432 (2012).
35. H. Hu, X. Yang, F. Zhai, D. Hu, R. Liu, K. Liu, Z. Sun, and Q. Dai, "Far-field nanoscale infrared spectroscopy of vibrational fingerprints of molecules with graphene plasmons," Nat. Commun. **7**, 12334 (2016).
36. X. Lin, Y. Xu, B. Zhang, R. Hao, H. Chen, and E. Li, "Unidirectional surface plasmons in nonreciprocal graphene," New J. Phys. **15**(11), 113003 (2013).
37. P. Li and T. Taubner, "Broadband subwavelength imaging using a tunable graphene-lens," ACS Nano **6**(11), 10107–10114 (2012).
38. B. H. Cheng, K. J. Chang, Y. C. Lan, and D. P. Tsai, "Actively controlled super-resolution using graphene-based structure," Opt. Express **22**(23), 28635–28644 (2014).
39. D. K. Efetov and P. Kim, "Controlling electron-phonon interactions in graphene at ultrahigh carrier densities," Phys. Rev. Lett. **105**(25), 256805 (2010).
40. Y. Cai, J. Zhu, Q. H. Liu, T. Lin, J. Zhou, L. Ye, and Z. Cai, "Enhanced spatial near-infrared modulation of graphene-loaded perfect absorbers using plasmonic nanoslits," Opt. Express **23**(25), 32318–32328 (2015).
41. G. W. Hanson, "Dyadic Green's functions and guided surface waves for a surface conductivity model of graphene," J. Appl. Phys. **103**(6), 064302 (2008).
42. L. A. Falkovsky and S. S. Pershoguba, "Optical far-infrared properties of a graphene monolayer and multilayer," Phys. Rev. B **76**(15), 153410 (2007).

Optics EXPRESS

43. P.-Y. Chen and A. Alù, "Atomically thin surface cloak using graphene monolayers," ACS Nano **5**(7), 5855–5863 (2011).
44. D. Rodrigo, O. Limaj, D. Janner, D. Etezadi, F. J. García de Abajo, V. Pruneri, and H. Altug, "Mid-infrared plasmonic biosensing with graphene," Science **349**(6244), 165–168 (2015).
45. P. B. Johnson and R. W. Christy, "Optical constants of the noble metals," Phys. Rev. B **6**(12), 4370–4379 (1972).
46. X. Fang, K. F. MacDonald, and N. I. Zheludev, "Controlling light with light using coherent metadevices: all-optical transistor, summator and invertor," Light Sci. Appl. **4**, e292 (2015).
47. W. Sun, Q. He, S. Sun, and L. Zhou, "High-efficiency surface plasmon meta-couplers: concept and microwave-regime realizations," Light Sci. Appl. **5**(1), e16003 (2016).
48. Y. Zhang, H. Wang, H. Liao, Z. Li, C. Sun, J. Chen, and Q. Gong, "Unidirectional launching of surface plasmons at the subwavelength scale," Appl. Phys. Lett. **105**(23), 231101 (2014).
49. M. Papaioannou, E. Plum, J. Valente, E. T. F. Rogers, and N. I. Zheludev, "Two-dimensional control of light with light on metasurfaces," Light Sci. Appl. **5**(4), e16070 (2016).
50. N. M. Idris, M. K. Gnanasammandhan, J. Zhang, P. C. Ho, R. Mahendran, and Y. Zhang, "In vivo photodynamic therapy using upconversion nanoparticles as remote-controlled nanotransducers," Nat. Med. **18**(10), 1580–1585 (2012).
51. M. He, X. Pang, X. Liu, B. Jiang, Y. He, H. Snaith, and Z. Lin, "Innenrücktitelbild: monodisperse dual-functional upconversion nanoparticles enabled near-infrared organolead halide perovskite solar cells," Angew. Chem. Int. Ed. **55**, 4367 (2016).
52. P. E. Hänninen, S. W. Hell, J. Salo, E. Soini, and C. Cremer, "Two-photon excitation 4Pi confocal microscope: Enhanced axial resolution microscope for biological research," Appl. Phys. Lett. **66**(13), 1698–1700 (1995).
53. S. Hell and E. H. K. Stelzer, "Properties of a 4Pi confocal fluorescence microscope," J. Opt. Soc. Am. A **9**(12), 2159 (1992).
54. L. Shao, B. Isaac, S. Uzawa, D. A. Agard, J. W. Sedat, and M. G. Gustafsson, "I5S: wide-field light microscopy with 100-nm-scale resolution in three dimensions," Biophys. J. **94**(12), 4971–4983 (2008).

1. Introduction

Surface plasmons (SPs), originated from the coupling of light and collective oscillations of free electrons in the metal, are evanescent electromagnetic waves existed at the interface between metal and dielectrics [1–3]. Their intriguing properties such as strong electromagnetic energy confinement and large in-plane momentum nature have been extensively exploited for applications in a variety of applications including biosensing, photolithography, sub-diffraction limited imaging and more [4–9]. SPs, own a higher wave-vector (k_{sp}) in comparison with the exciting light in some cases, are good candidates for optical resolution improvements. Recently, the application of SPs in super-resolution has been extensively studied in the near-field including examples such as perfect lens, superlens and hyperlens [10–12]. Even more recently, plasmonic structured illumination microscopy (PSIM), a far-field microscopy technique has been introduced. This approach utilizes SPs to further improve far field imaging resolution [13–18]. In those works, plasmonic interference pattern was used as the illumination pattern to realize a lateral resolution enhancement of a fluorescence image. As the resolution of this method relies on the spatial frequency of the SP illumination pattern, an improvement of more than twice in resolution has been achieved in comparison with conventional epifluorescence microscopy, both numerically and experimentally. Clearly, higher k_{sp} is critical for achieving higher resolution. Previous studies show that subwavelength metallic structures can be applied to excite SPs with a higher wave-vector [14,16,19]. There are many efforts to seek for higher k_{sp}, including 2D silver-silicon nitride-air platforms [20], hyperbolic metamaterials [21–25], noble metal meta-structure [26,27], etc. In this context, graphene shows an outstanding electric, thermal and optical properties in terahertz and infrared domains and therefore can support SPs with an ultra-high wavevector for applications in transformation optics, nano-imaging and tunable metamaterials [28–32]. Graphene can also be used as a nano-ruler based on Förster resonance energy transfer (FRET) in application for bio-imaging [33,34]. Thanks to its inherent properties, combined with recent advances in nanofabrication, graphene plasmonics have made a remarkable progress [35–38]. In particular, given the fact that high doping density has already been achieved in recent experiments [36–39], the working frequency of graphene plasmonics

Optics EXPRESS

could be extended to the near infrared domain or even the visible light spectrum which makes it even more attractive for imaging applications.

In this work, we propose a hybrid graphene on meta-surface structure (GMS), which can support ultra-high k_{sp}. First, the finite-difference time domain (FDTD) method was employed to analyze GMS structure and it is found that the SW-SPs with an 11 nm period can be achieved on graphene for a 980 nm illumination wavelength. Furthermore, it was demonstrated theoretically that the GMS structure can be applied in the plasmonic structured illumination microscopy method and an imaging resolution of 6 nm can be achieved, which serve as a clear indication for the great potential of this method in imaging resolution enhancement for optical super-resolution imaging.

2. Methods and structure description

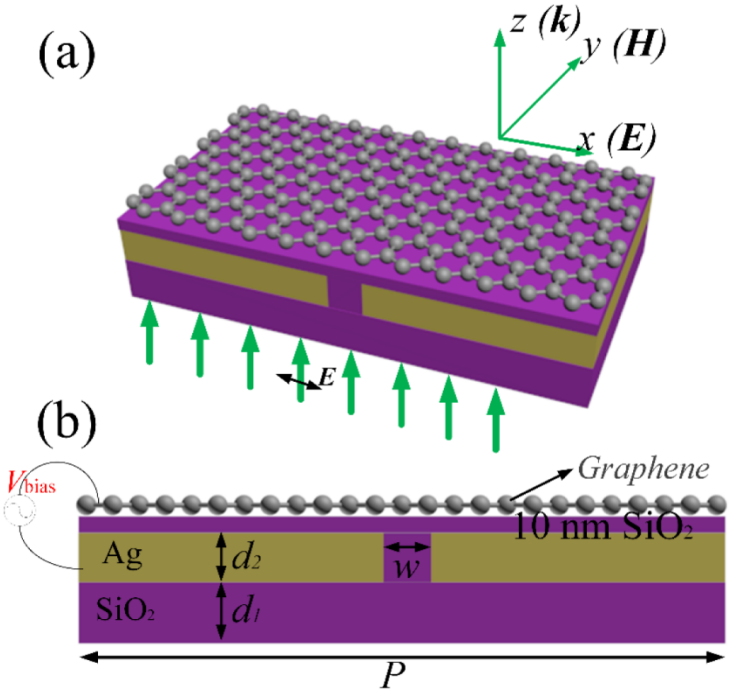

Fig. 1. The schematic diagram of the hybrid graphene on meta-surface structure. (a) The perspective view and (b) the cross sectional view of the GMS. V_{bias} denotes the control voltage for setting the chemical potential of graphene.

Figure 1 shows the proposed GMS structure which consists of a single layer of graphene deposited on a SiO_2/Ag/SiO_2 multilayer structure. Figures 1(a) and 1(b) show the perspective and cross sectional views of a unite cell of the GMS structure, respectively. As can be seen, each unit cell of the GMS structure consists of four layers. The thickness of the flat SiO_2 substrate is d_1 = 200 nm. The other layers of the GMS are the key for achieving high $k_{sp.}$. A thin layer of silver film with a thickness of d_2 = 50 nm is deposited on the SiO_2 substrate and then covered by a 10 nm SiO_2 film. There is a nano-slit with a width W = 30 nm in x direction and an infinite length in y direction defined in Ag film and filled with SiO_2. The nano-slit is used to couple the incident light into SPs and to excite the graphene plasmonic mode [40]. The unit cell is repeated in both x and y directions with the same period of P = 350 nm.

For the graphene layer, the surface conductivity σ_g can be calculated by Kubo model of conductivity [41,42]:

Optics EXPRESS

$$\sigma_g = \frac{ie^2 k_B T}{\pi\hbar^2(\omega + i/\tau)}\left(\frac{\mu_c}{k_B T} + 2\ln\left(e^{-\frac{\mu_c}{k_B T}} + 1\right)\right) + \frac{ie^2}{4\pi\hbar}\ln\left|\frac{2\mu_c - \hbar(\omega + i/\tau)}{2\mu_c + \hbar(\omega + i/\tau)}\right| \quad (1)$$

where e is the electron charge, k_B is the Boltzmann constant, T is the Kelvin temperature, $\hbar$ is the reduced Planck constant, ω is the radian frequency, μ_c is the chemical potential, and τ is the electron-phonon relaxation time, respectively. The relaxation time τ can be obtained by using:

$$\tau = \frac{\mu_c \mu}{e v_F^2} \quad (2)$$

where μ is the DC mobility, and v_F is the Fermi velocity. In the model and simulations to be followed, it is assumed that the graphene is an anisotropic dispersive dielectric material and its relative permittivity ε_g can be represented as:

$$\varepsilon_g = 1 + i\frac{\sigma_g}{\varepsilon_0 \omega \Delta} \quad (3)$$

where ε_0 is the permittivity of vacuum and Δ denotes the graphene thickness. In order to allow for proper convergence, the graphene thickness Δ is chose as 1 nm [35–38] in our simulation. From Eqs. (1)-(3), it is found that the permittivity of graphene depends on the surface conductivity, which can be electrically tuned by bias voltage. In the simulation, the parameters for graphene are: T = 300 K, $v_F = 10^5$ m/s, μ = 10000 $cm^2V^{-1}s^{-1}$. Therefore, the surface conductivity σ_g mainly depends on ω and μ_c. As D.K. Efetov *et al* already demonstrated that a chemical potential μ_c = 2.2 eV is possible [39], the value of the chemical potential μ_c can be tuned from 0.1 eV to 2.2 eV in the model.

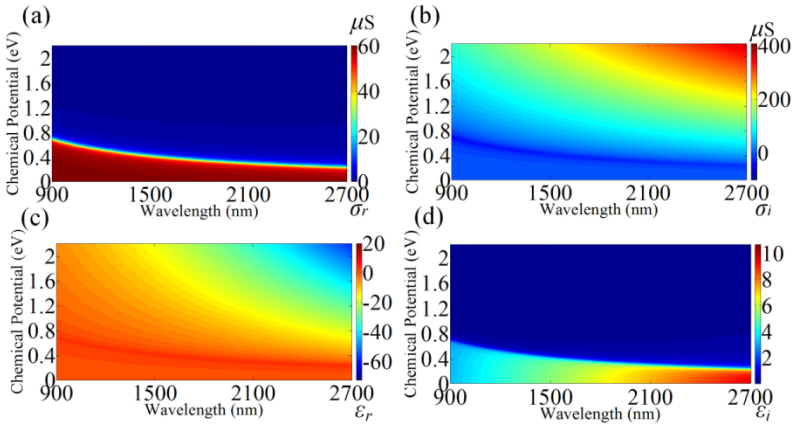

Fig. 2. Dispersive optical properties of graphene as a function of chemical potential in near infrared waveband. (a) The normalized real and (b) imaginary part of surface conductivity of graphene, respectively. (c) The real and (d) imaginary part of permittivity of graphene, respectively.

The chemical potential μ_c can be determined by applying a bias voltage as shown in Fig. 1(b). According to Eq. (1), the real part σ_r and imaginary part σ_i of graphene surface conductivity in near infrared waveband were calculated and shown in Figs. 2(a) and 2(b), respectively. It can be clearly seen that the imaginary part σ_i of graphene surface conductivity can have positive or negative values for different wavelengths and chemical potentials. From Eq. (3), the relative permittivity of graphene as a function of μ_c and free space wavelength λ

Optics EXPRESS

can also be calculated, as presented in plots of Figs. 2(c) and 2(d). As shown in Fig. 2(c), for a specific λ, ε_r is positive when $\mu_c<\hbar\omega/2$. Under this condition, the graphene can be regarded as dielectric and no longer supports transverse magnetic (TM) SPs. However, when $\mu_c>\hbar\omega/2$, ε_r starts to change from positive to negative, the graphene then behaves as a metallic layer. It can be found that ε_i decreases slowly as μ_c increases when $\mu_c<\hbar\omega/2$ in Fig. 2(d). And when μ_c becomes larger than $\hbar\omega/2$, ε_i has a dramatic drop. This variety of optical properties makes graphene an ideal candidate in applications including invisibility cloaks [43] and plasmonic sensors [44].

By employing a commercial finite-difference time domain (FDTD) simulation software (Lumerical FDTD Solutions), the GMS structure was modeled and analyzed. Three-dimensional (3D) simulations were performed with a TM polarized plane wave incidents in z direction at 900-2700 nm waveband. The incident angle was set as $\theta_0 = 0$, i.e. normal incidence. The inset of Fig. 1(a) shows the direction of incident waves with respect to the perspective of the proposed GMS structure. Periodic boundary conditions (PBC) were applied in both x and y directions and perfectly matched layer (PML) boundary condition was applied in z direction. The FDTD region was set as $0.35 \times 0.35 \times 1.3$ μm^3. In the regions where SPs exist, finer meshes with smaller cubes of $1 \times 1 \times 1$ nm^3 were applied. Smallest cubes of $1 \times 1 \times 0.1$ nm^3 were applied in the graphene layer to maintain the accuracy and stability of FDTD calculations. A coarse meshing was constructed elsewhere. In the software, the optical constants of Ag are taken from literature [45].

3. Results and discussion

Figure 3(a) shows the real and imaginary part of permittivity of graphene for $\mu_c = 2$ eV, which is extracted from Figs. 2(c) and 2(d). The distribution of the electric field of a unite cell in different planes for wavelength $\lambda = 980$ nm was calculated and shown in Figs. 3(b)-3(d). It can be clearly seen that the standing wave interference patterns of the SPs exist along the x direction. Figure 3(b) shows that the electric field distribution in plane $y = 0$. In addition, the color bar shows the electric field intensity. One can see clearly that the standing wave (SW) pattern of the SPs existed well at the SiO_2/graphene and graphene/air interfaces. And the SW-SPs was not existing in the silver/SiO_2 interface. The distribution of electric field in plane $z =$ 113 nm (2 nm above the graphene layer) is shown in Fig. 3(c). Since the nano-slit in Ag film is infinitely long along the y-direction, we can have a one-dimensional SW-SPs pattern in x direction. Figure 3(d) is the electric field distribution along the blue dashed line in Fig. 3(c). Only electric field distribution along half of the blue dashed line is plotted due to the symmetry of the structure. As can be seen from the figure, the period of the SW-SPs is as small as 11 nm. Consequently, the period of SW-SPs wave is only about one 89th of $\lambda_0 = 980$ nm in our GMS model. In order to demonstrate the advantage of graphene layer in the SPs wave-vector improvement, the simple silver-SiO_2 structure without the graphene layer on the top was also simulated. The prospective view of the structure was shown in Fig. 3(e). Figure 3(f) shows the electric field distribution in plane $y = 0$. From this figure, it can be found that SPs does not exist at the interface of air/SiO_2. In comparison with the model with graphene, it can be concluded that it is the graphene SPs plays an important role in supporting the ultra-high wave-vector. From Fig. 3(b), we can find the SPs to be confined at the interfaces of graphene/SiO_2 and graphene/air. And the intensity of electric field at the positions of nanoslits in Ag film is more than 1.5 I_0 (I_0 is the intensity of incident wave). Therefore, the physical mechanism of GMS is based on localized surface plasmon enhancement and graphene plasmonics. Localized surface plasmon resonance (LSPR) is excited by the nanoslits in Ag film. The momentum mismatch between the graphene SPs and the excitation source is compensated by the Ag nanoslits. Hence, the graphene SPs with ultra-high wave-vector are excited.

Optics EXPRESS

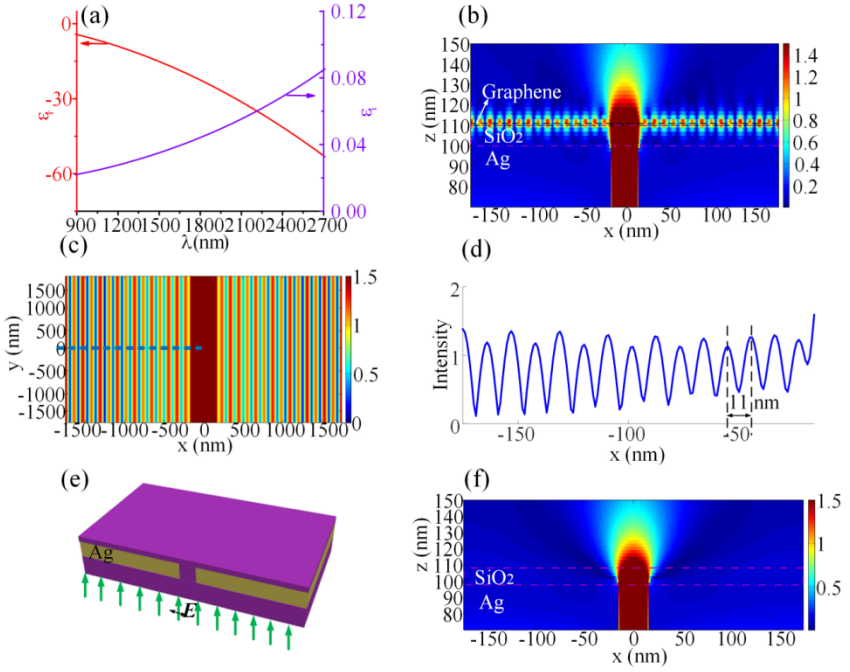

Fig. 3. (a) The real and imaginary part of permittivity of graphene for μ_c = 2 eV. (b) The distribution of the electric field in y = 0 plane. (c) The distribution of the electric field in z = 113 nm plane. (d) The distribution of the electrical field intensity along the blue dashed line. (e) The perspective schematic diagram of the simple silver-SiO_2 structure. (f) The distribution of the electric field of the simple silver-SiO_2 structure in y = 0 plane, with the same parameters of GMS.

To further understand the physical mechanism related to obtaining graphene SPs with ultra-high wave-vector, the wave-vector of SPs supported by a stack of graphene-SiO_2-air is derived analytically by Maxwell's electromagnetic theory. Figure 4(a) shows the simplified structure. A TM polarized light incidents normally along z axis. It is hypothesized that the SPs is already excited on graphene layer.

From the Maxwell equations, one can extract the components of the electric and magnetic fields. The similar analytical equations can be found in [26].

By also applying boundary conditions, one can obtain the following equation,

$$\frac{k_{2z}/\varepsilon_2 + k_{1z}/\varepsilon_1}{k_{2z}/\varepsilon_2 - k_{1z}/\varepsilon_1} = e^{-2k_{2z}d_2}\,\frac{k_{2z}/\varepsilon_2 - k_{3z}/\varepsilon_3}{k_{2z}/\varepsilon_2 + k_{3z}/\varepsilon_3} \tag{4}$$

In the above equation,

$$k_{iz} = \sqrt{\beta^2 - k_0^2\varepsilon_i} \quad (i = 1\text{-}3) \tag{5}$$

Where k_{iz} and β stand for the components of the wave vector of SPs in the *ith* layer along z and x direction, respectively, k_0 represents the free-space wave-vector and d_i (i = 1-3) stands for the thickness of the *ith* layer.

Optics EXPRESS

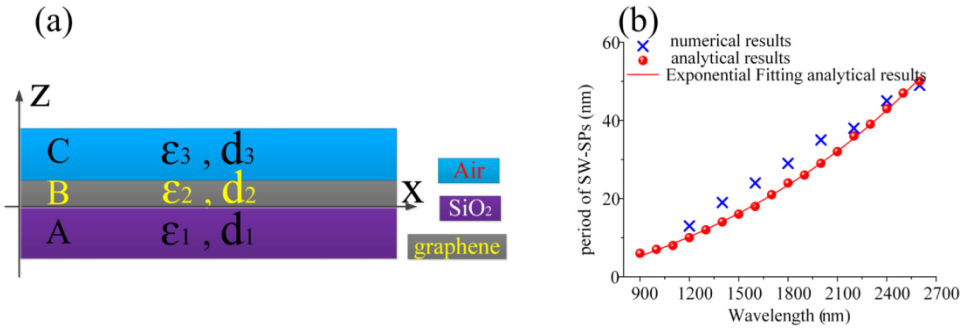

Fig. 4. (a) The schematic diagram of the structure used in the analytic model. ε_i and d_i stand for the permittivity and thickness of the material in each layer. (b)The period of plasmonic interference pattern as a function of the incident wavelength as obtained by analytic and numerical methods.

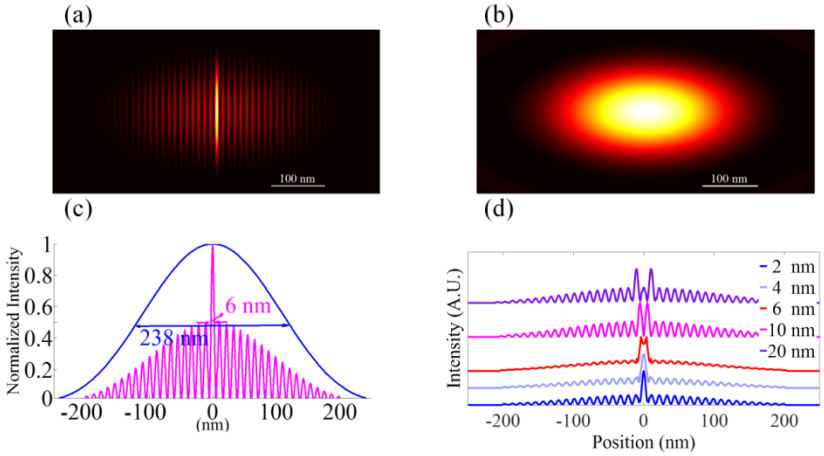

Fig. 5. The simulation results of the imaging performance for GMS model. Point spread function of (a) reconstructed image in *x*-direction, (b) a diffraction-limited system, (c) FWHM comparison between conventional lens-based microscopic image (blue curve) and the super-resolution image by sing the GMS (magenta line) in PSIM, (d) Illustration of resolving capability of GMS-PSIM of two POs separated with different distances of 2, 4, 6, 10 and 20 nm in *x*-direction.

Subsequently, the different permittivity and thickness of each layer were taken into account and the wave vector of graphene SPs at 900-2700 nm waveband can be calculated by combining Eqs. (4) and (5). The results are shown in Fig. 4(b). The circle and cross points represent the analytical and numerical results, respectively. In general, the period of SW-SPs increases with the excitation wavelength and follows an Exponential distribution form. From this figure, one can find that the numerical results agree with the analytical ones fairly well with a maximum deviation of 6 nm in period. As a result, the ultra-high wave vector of the GMS model is confirmed by both numerical and analytical methods.

In our GMS model, the nanoslit array is used to assist to excite one-dimensional SW-SPs on graphene layer. Other coupling elements such as half circle slits and the designed metasurfaces can also be applied to achieve additional forms of SPs interference patterns [46–49]. As can be seen from Fig. 3(b), the intensity of the SW-SPs at the graphene/air interface is about 1.2 I_0, which surpasses that obtained by other metamaterials [25]. It means that the light intensity is enhanced for graphene surface plasmonic wave in comparison with the traditional metamamterials composed by noble metals, which is beneficial e.g. to the imaging of the biological samples in terms of enhancing the signal to noise ratio.

Optics EXPRESS

The proposed GMS model can be used as a platform for super-resolution imaging with a PSIM mode. To demonstrate its imaging performance, the images of point objects (POs) were tested. POs with a step function for intensity are placed upon the graphene layer. The SW-SPs pattern serves as the structured illumination pattern to illuminate the POs. In this work, only super-resolution image in *x*-dimension is reconstructed due to the illumination patterns along *x* direction. In order to generate a reconstructed image, the same method in our previous work is taken and the details can be found elsewhere [26].

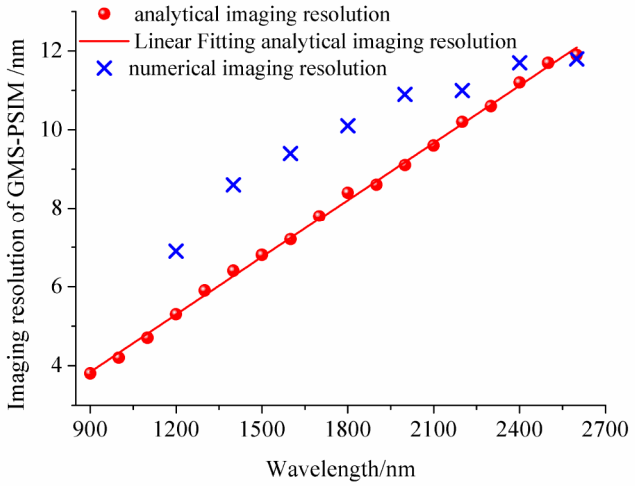

Fig. 6. The analytical and numerical imaging resolution of GMS-PSIM in the near-infrared waveband. The black circles represent the analytical results, the red line stands for the linear fitting of the analytical results and the blue crosses represent the numerical results.

In our numerical model, a 10 nm PO is used to obtain the point spread function (PSF) of the conventional microscopy and the GMS-PSIM systems. The PO with emission wavelength 655 nm is selected [50,51]. The fluorescent signal from the PO is assumed to be detected by an immersion oil objective with a NA of 1.42. The results are shown in Figs. 5(a)-5(c). Figure 5(a) shows the reconstructed image of the PO in the GMS-PSIM system. Figure 5(b) shows the image of the PSF of the PO illuminated by a conventional homogeneous pattern. A comparison of the PSF profile across the *x*-axis of Figs. 5(a) and 5(b) was shown in Fig. 5(c). From Fig. 5(c), it can be found that the FWHM of the conventional microscopy is about 238 nm. However, the FWHM is only about 6 nm for GMS-PSIM. Therefore, the imaging resolution has been improved by about 39.6 folds by introducing the GMS structure in PSIM. Furthermore, the resolving capability of GMS-PSIM can be obtained by imaging two point POs with different separation distances as shown in Fig. 5(d). These cross sectional profiles show the imaging enhancement in *x*-direction by using a one-dimensional SW-SPs pattern. Based on the Rayleigh criterion, it is shown that GMS-PSIM is capable to resolve two objects separated by about 6 nm. However, similar to other super-resolution methods based on interference methods, there exist sidelobes surrounding the central spots in Figs. 5(b) and 5(d). Appropriate post-processing methods should be used to eliminate these artifacts so that the image quality can be further improved [52–54].

From Fig. 4(b), on can find the deep subwavelength SPs interference pattern can be achieved through GSM in the waveband of 900-2700 nm. Therefore, we can expand the excitation wavelengths to the near-infrared waveband. The resolution of PSIM is $\lambda_{em}/(2\mathrm{NA} + 2\mathrm{NA}_{\mathrm{eff}})$ [17,18], in which λ_{em} is the emission wavelength of the POs and $\mathrm{NA}_{\mathrm{eff}} = k_{sp}/k_0$ with k_0 stands for the wave vector of the excitation light. It is assumed that the emission wavelength

Optics EXPRESS

of POs is 655 nm. After using the analytical results of period of SW-SPs in Fig. 4(b) and the equation of the resolution of PSIM, the imaging resolution are calculated as shown in Fig. 6. It can be found from the curve that the value of the imaging resolution becomes larger with the increase in the excitation wavelength in a linear form. We can also obtain the numerical imaging resolution, represented as blue cross in Fig. 6. From this figure, one can find that the numerical results agree with the analytical ones well with a maximum deviation of 2.2 nm in imaging resolution. Therefore, the optical imaging resolution can be tuned through changing the excitation wavelength.

4. Conclusions

In summary, a hybrid graphene on meta-surface structure was demonstrated in this work. This structure features a single graphene layer integrated on a multilayer of SiO_2/Ag/SiO_2 platform. In comparison with traditional multilayer metamaterial structure and noble metal meta-structures, the proposed new structure is more elegant and in particular can support SPs wave with an ultra-high wavevector. The dispersion relation of the structure is presented. It is found that the period of the SW-SPs pattern is only 11 nm when the wavelength of incident light is 980 nm. The application of this deep subwavelength SPs interference pattern to super-resolution optical imaging was discussed. It was found that the reconstructed image shows a 39.6-folds improvement on the resolution in comparison with that of the conventional lens-based microscopy. The imaging resolution of GSM-PSIM can be tuned in the near-infrared waveband through changing the wavelength of the incident wave. All of these merits of the new structure show great potential for variety of applications, e.g. in the field of super-resolution biomedical imaging.

Funding

National Natural Science Foundation of China (NSFC) (61361166004, 61475156); Technology Department of Jilin Province (20140519002JH).